Geophysical Journal International

Geophys. J. Int. (2014) **196,** 1889–1905
Advance Access publication 2014 January 10

doi: 10.1093/gji/ggt504

Structure of the subduction transition region from seismic array data in southern Peru

Kristin Phillips and Robert W. Clayton

Division of Geophysics, Caltech Seismological Laboratory, MS 252-21*, Pasadena, CA* 90240*, USA. E-mail: k.phillips.alonge@gmail.com*

Accepted 2013 December 11. Received 2013 December 7; in original form 2013 August 28

SUMMARY

Data from three seismic arrays installed in southern Peru were analysed using receiver functions from *P*, *PP* and *PKP* wave phases, in order to image the subducted Nazca slab. The arrays cover the transition region from flat slab subduction in central Peru to normal subduction with an angle of about 30° further south. A previous study used data from the first array in the normal subduction region to image the Moho depth and slab, and showed the existence of a mid-crustal structure at 40 km depth that is suggested to be a possible underthrusting of the Brazilian shield. Here, we discuss new observations from the other two arrays that span the transition between the two subduction regimes and the flat subduction region. The results provide an image of the flattened slab from the coast to approximately 300 km inland and also across the transition region from flat to 30° subduction, which appears to be a bend rather than a tear in the slab. In the flat slab region, the slab is well defined near the coast and flattens out at 100 km depth beneath the Altiplano. The slab appears to start flattening some 400 km in advance of the subduction of the Nazca Ridge and the flattening is maintained for 1300 km after its passage. The Moho begins at a depth of around 30 km near the coast and has a maximum depth of 75 km beneath the Altiplano, consistent with the results of the other arrays. Both arrays also show a positive impedance mid-crustal structure at 40 km depth, which if explainable by underthrusting of the Brazilian shield, would add further support to the observations from the normal subduction region and show the northward and westward extent of the signal. The underthrusting hypothesis would explain the missing crust from the shortening budget needed to support the Altiplano. The *Vp*/*Vs* ratios for both arrays exhibit average values between 1.73 and 1.75 indicating a lesser likelihood that there is a high degree of partial melting or magma bodies at depth in this region. The receiver function results provide new imaging of the flat slab and transition from normal to flat slab subduction which allows for comparison of different subduction regimes.

Key words: Seismicity and tectonics; Continental margins: convergent; Crustal structure.

1 INTRODUCTION

The dip of the subducted Nazca Plate beneath southern Peru changes from shallow or flat slab beneath central Peru to a steeper dip angle ('normal' subduction) of around 30° beneath southern Peru. This transition is evident in the seismicity (Barazangi & Isacks 1976; Suarez *et al.* 1983; Grange *et al.* 1984; Cahill & Isacks 1992), and by a gap in the arc volcanism (McGeary *et al.* 1985; Gutscher *et al.* 1999a, 2000b). Adakitic magmas have also been associated with flat slab regions (Gutscher *et al.* 2000a) and have been reported in southern Ecuador/northern Peru (Beate *et al.* 2001). They are suggested to result from partial melting of subducted oceanic crust. Besides the observed correspondence between adakites and flat slab regions, the partial melting resulting in such magmas could also be a result of slab tearing at the transitions from flat slab to a steeper dip angle (Yogodzinski *et al.* 2001). The lack of reported adakites in southern Peru gives some indication that the southern transition is slab bending rather than a tear. The change in dip is coincident with the subduction of Nazca Ridge. This is one of three zones of slab-dip changes along the western margin of southern America. In central Chile, the subduction of the Juan Fernandez Ridge is cited as the cause of the flatten along its subduction trajectory (Pilger 1981; von Huene *et al.* 1997; Gutscher *et al.* 2000b), and the study of Anderson *et al.* (2007) shows that the zone of flattening tightly conforms to the shape of the ridge. In Equador, the Carnegie Ridge also apparently causes the slab to flatten (Gutscher *et al.* 1999b).

Various mechanisms have been proposed as to the cause of flat slab subduction. Some authors have noted a correlation between regions of flat slab subduction and the presence of thickened oceanic crust such as that due to a subducting plateau or ridge which could

increase the buoyancy of the subducting slab (Gutscher *et al.* 2000a). Gutscher *et al*. (1999a) proposed that the length of flat subduction in Peru was due to buoyancy effects resulting from two subducting bodies; the Nazca Ridge and a previously unknown impactor referred to as the Inca Plateau which is believed to be the mirror image of the Marquesas Plateau although recent plate movement reconstructions call into question the proposed location and timing of the Inca Plateau (Skinner & Clayton 2013). Both plateaus were suggested to have formed at the Pacific–Farallon spreading centre based on tectonic reconstructions. According to Hampel (2002), the Nazca Ridge originally began subducting at 11°S at around 11.2 Ma. Since then it has been sweeping south and presently has a migration rate of around 43 mm a^{-1} (Hampel 2002). The region of flat subduction in Peru corresponds to the area swept out by the Nazca Ridge. Thus, the Nazca Ridge may have had an impact on the evolution and shape of the subduction zone. In addition to buoyancy effects caused by a subducting ridge or plateau, other factors could influence flat subduction such as the age of the lithosphere being subducted (Sacks 1983), delay in the basalt to eclogite transformation (Pennington 1984; Gutscher *et al.* 2000b), absolute motion of the upper plate (Olbertz *et al.* 1997), the convex curvature of the Peruvian margin (Bevis 1986; Cahill & Isacks 1992), intraplate hydrostatic suction (Jischke 1975) or cycles of flat subduction caused by rebound after a steepening slab breaks off (Haschke *et al.* 2002).

Modelling has been done in several studies to address the relative importance of different causes for flat slab subduction. van Hunen *et al*. (2002a) suggested that relative motion of the upper plate could be equally or more important than plateau subduction based on numerical studies; however, this is a factor that is present in the region of normal subduction as well. The dominant mechanism for flat slab subduction needs to be considered independently for each subduction zone since some factors are present in both normal and flat slab regions while other factors can be observed in only some flat slab regions and not in others. One of the puzzling aspects of the flat subduction in southern Peru is the fact that the slab does not return to a normal dip angle after the impactor has passed. This contrasts with central Chile where the slab returns to normal dip at a distance of about 150 km on either side of the track of the Juan Fernandez Ridge (based on contours from Anderson *et al.* 2007).

In this study, we examine the details of the transition zone between normal and flat subduction using dense seismic arrays, which include instruments both in the flat slab zone as well as an array parallel to the trench to sample the subduction transition. The array in the flat slab region near the Nazca Ridge provides an opportunity to study the effect of the Nazca Ridge on the subduction zone in southern Peru. A previous study (Phillips *et al.* 2012) has described the results of a line (Line 1, Fig. 1) that is in the normal dip part of the zone. It succeeded in imaging the slab down to 250 km, and

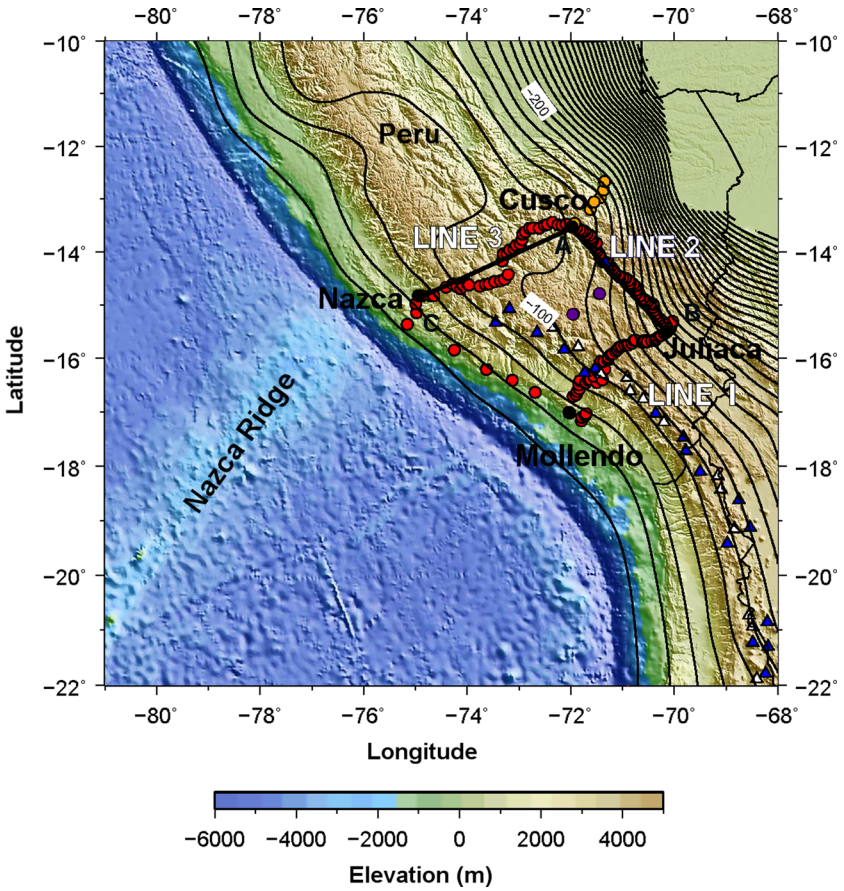

Figure 1. Location of the seismic arrays in southern Peru as denoted by red circles. Added stations from the PULSE and CAUGHT experiments are shown as orange and purple circles, respectively. The topography and bathymetry show the incoming Nazca Ridge and the Altiplano of the Andes. Slab contours are based on fits to seismicity and comes from the Slab 1.0 model (Hayes *et al.* 2012). Active and dormant volcanoes are denoted by white and blue triangles. The three seismic arrays are labelled 'Line 1', 'Line 2' and 'Line 3'. Line 1 is located in the region of normal subduction, Line 2 samples the transition from normal to flat slab subduction and Line 3 is in the flat slab region. The black lines along Lines 2 and 3 with endpoints labelled A, B and C correspond to cross-section profiles in Fig. 2.

found a mid-crustal velocity increase at about 40 km depth suggested to be underthrusting by the Brazilian shield. In this study, we expand on those results by presenting details of the transition and flat slab subduction regions.

Receiver function studies performed here provide details of the structure of the subduction system including Moho depth and shape of the slab as well as velocity information such as *Vp*/*Vs* ratio. Corresponding images show the transition from normal to flat slab subduction and the shape of the slab in the flat slab region, which is affected by the subducting Nazca Ridge. The structure of the flat slab region is compared to the study of the normal subduction regime. The slab geometry is important for simulations of flat slab evolution such as those found in Manea *et al*. (2012) and O'Driscoll *et al*. (2012).

2 METHODS

2.1 Stations and data

Three lines of broad-band sensors were installed as part of the Peru Subduction Experiment (PeruSE) as seen in Fig. 1. The first line (Line 1) deployed perpendicular to the trench from Mollendo on the coast to Juliaca near Lake Titicaca, samples the region of normal subduction dip (Phillips *et al.* 2012). The second seismic array (Line 2) runs parallel to the trench from Juliaca to Cusco sampling the transitional region where the subduction regime changes to shallow subduction. It includes 50 broad-band seismic stations over a distance of about 300 km resulting in an average station spacing of about 6 km. Line 3 is perpendicular to the trench starting on the coast near the city of Nazca and runs inland through Cusco for 509 km. It consists of 40 stations from the PeruSE network plus five stations from the PULSE network (Eakin *et al.* 2011). Line 3 is located near where the Nazca Ridge is subducting beneath South America and samples the flat slab region. In addition, two stations from the CAUGHT network (Ryan *et al.* 2011) that are in the interior of the box defined by the networks described above are used.

The flat slab and the transition from normal to flat slab subduction can be roughly delineated by the seismicity of the Wadati–Benioff zone as is shown in Fig. 2. Event locations are from the International Seismological Centre (ISC) reviewed catalogue. The black lines show an average value for slab location based on best fit to seismicity. The seismicity shows the slab flattening out at 100 km depth beneath the Altiplano in the flat slab region and the shape of the curve in the transition region between Cusco and Juliaca.

Teleseismic data collected by the array were used in receiver function studies. Earthquakes between 30° and 90° away from Peru were used to make receiver functions based on the *P*-wave arrival. However, since many events are located beyond 90° from Peru, *PP* and *PKP* phases were also analysed for events occurring at distances greater than 90° distance from Peru. *PKP* phases are used at distances between 143° and 180° and can be useful for detecting dipping interfaces. For Line 2, a total of 73 events using the *P*-wave phase, 175 *PP* and 50 *PKP*-wave phase events were used in this study. For Line 3, 50 *P* wave, 106 *PP* and 21 *PKP* phase events were used. To ensure higher signal to noise, events are of magnitude 5.8 or greater for distances less than 90° from Peru and greater than magnitude 6.0 for distance greater than 90°. The data were generally bandpassed from 1 to 100 s, but this was narrowed to 2–100 s for some distant events with higher apparent noise. Data were included if the signal-to-noise ratio appeared adequate for both the raw seismic data and resultant receiver functions.

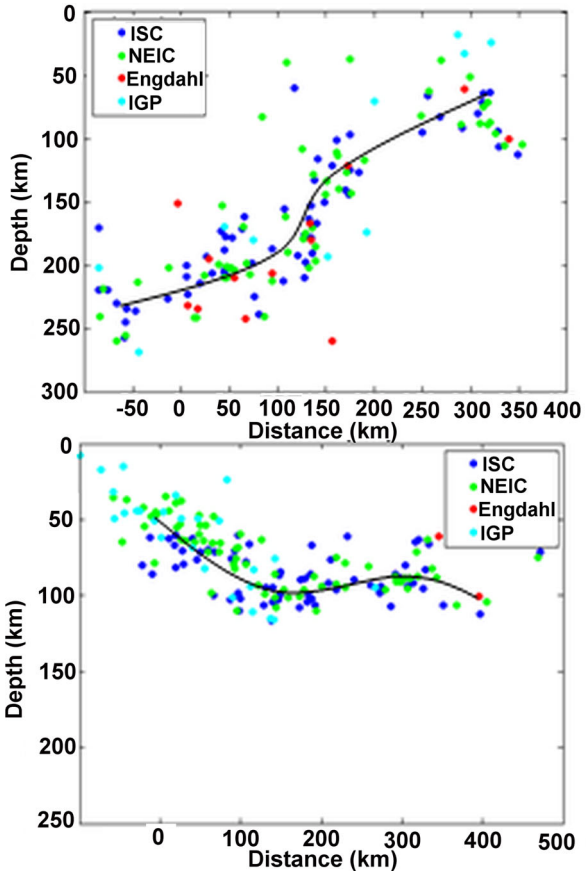

Figure 2. Seismicity cross-sections along the projections of Lines 2 and 3 shown as black lines in Fig. 1. Earthquakes locations are shown for available catalogues including the ISC reviewed catalogue (International Seismological Centre 2010), NEIC (National Earthquake Information Center), the Engdahl centennial catalogue (Engdahl & Villaseñor 2002) and IGP (Instituto Geofisico del Peru) as reported on their recent earthquakes website. The black lines show the estimated slab location from the best fit to the seismicity. (a) Seismicity cross-section parallel to the trench from Juliaca to Cusco as shown as black line B–A in Fig. 1. Cusco is located in the region of flat slab subduction while Juliaca further south is in the region of normal subduction. (b) Seismicity cross-section from Nazca to Cusco in the region of flat slab subduction shown by line C–B in Fig. 1.

2.2 Receiver functions

Receiver functions were formed using the method described in Langston (1979) and Yan & Clayton (2007). Mantle and source effects are minimized by deconvolving the radial with the vertical component in the frequency domain (Langston 1979; Ammon 1991). Time-domain iterative deconvolution (Ligorría & Ammon 1999) was also tried, but produced noisier results. Receiver functions were stacked using the method of Zhu & Kanamori (2000) using multiple events from a similar backazimuth for each station to perform stacks. A maximum weighted summation function for stacking over the Moho and multiple arrivals provide estimates for depth to the impedance contrast and the *Vp*/*Vs* ratio. Average crustal *P*-wave velocities used in the estimate of depth and *Vp*/*Vs* from stacking of receiver functions for each station were derived mostly from averages of the 3-D *P*-wave velocity structure of Cunningham & Roecker (1986) for southern Peru. Their model was also compared with more recent velocity models such as the model of Dorbath *et al*. (2008) from northern Chile. Uncertainty in the stacking method described above is given by the 95 per cent maximum

contour. Estimates of depth uncertainty due to uncertainty in the velocity model used for stacking are on the order of 2 km or less based on performing stacks with variations in average crustal *Vp* of up to 0.2 km s^{-1} from the velocity model used.

2.2.1 Receiver function imaging methods

Several different imaging and migration approaches were tested in order to image the receiver function data. Although all the imaging methods show consistency in the major arrivals such as the Moho, the various methods can highlight or bring out different features in the data and are useful to compare.

One imaging method uses backprojection to plot receiver function amplitudes along rays projected in the direction from which the energy originated. The initial velocity model for converting receiver function time to depth was a simple layered velocity model based on IASP91 but the model was tested against one with a thicker crust to better reflect expectations for the Andes. The change was not observed to affect resultant depths in images significantly. The backprojection uses information such as the ray parameter and back-azimuth to calculate the arrival angle at the station and estimate the distance from the station at a given depth. Examples of images using this method can be seen in Figs 6(a) and 11(a)–(c) as discussed in the Section 3. A related but slightly different approach uses common conversion point (CCP) stacking in which the Moho piercing point is estimated using backprojection. The array is divided into distance bins and at each distance the stack of all receiver functions with a Moho piercing point at that distance is plotted vertically as a function of depth. This is different from the other imaging approach where each point in the image is a stack of all rays that pass through that point. Examples of CCP stacking can be seen in Figs 4 and 6(b).

In addition to backprojection and CCP stacking, a migration of *P*-to-*S* converted phases using a Kirchoff-style migration is done by assuming a conversion occurs at every possible scattering point to calculate traveltimes. Corresponding amplitudes are stacked to form an image. A simple half-space starting model for the traveltime inversion uses an average crustal *P*-wave velocity of 6.3 and the average *Vp*/*Vs* ratio of 1.75. The velocity was varied to test sensitivity of the migration results to the velocity changes. An example of receiver function migration can be seen in Fig. 5. Further details of the receiver function methodology and imaging are discussed in the Supporting Information and in Phillips *et al.* 2012.

2.3 Finite difference modelling

A simple 2-D velocity model was used to produce synthetic receiver functions using a 2-D finite difference code (Kim *et al.* 2010) to compare with receiver function results for both Lines 2 and 3. The model for Line 2 is 300 km wide in distance and 250 km in depth. It has an average crustal *P*-wave velocity of 6.3 km s^{-1} with a mid-crustal velocity jump to 6.6 km s^{-1}. The velocity jump is constrained by the amplitude of the mid-crustal arrival. The mantle wedge is taken as having an average velocity of 7.7 km s^{-1} and the subducting oceanic crust as 7.0 km s^{-1} (Abers 2000; Abers *et al.* 2006; Kim *et al.* 2010). The underlying mantle is taken as having an average velocity of 8.0 km s^{-1} down to 250 km. Synthetic receiver functions are produced by modelling plane waves with variable ray parameters to simulate teleseismic sources. The finite difference synthetics are of comparable frequency content to the teleseismic data used to produce receiver functions in this study. Synthetic receiver functions are produced using a standard time-domain deconvolution algorithm.

3 RESULTS

3.1 Line 2 results: transition from normal to flat slab subduction

Line 2 samples the transition from normal to flat subduction. On the SE end (near Lake Titicaca) the slab is at a depth of approximately 215 km, while on the NW end (near Cusco) the slab is at a depth of 100 km. An image of the Moho and the slab can be seen in the receiver functions shown in Fig. 3(a). The receiver function signal from the slab is usually defined as negative and positive receiver function pulses at the top and bottom of the subducting oceanic crust. In some cases, the double pulse signal is detectable while in some cases either a positive or negative signal is dominant. In the case of Line 2 (Fig. 3a), the region where the slab is expected based on seismicity slab contours (see black line in Fig. 3a) contains a broad region of negative impedance with a shape that bends upwards as expected of the slab signal as delineated by the dotted yellow line. Also observable is a mid-crustal positive impedance signal at a depth of about 40 km, which was interpreted by Phillips *et al*. (2012) to result from the underthrust Brazilian shield. The strength of the mid-crustal signal relative to the Moho can be seen in the Supporting Information which shows that a very similar Moho and mid-crustal signal are seen at multiple stations across the array. Both features appear to be relatively flat and the Moho has an average depth between 70 and 75 km beneath the Altiplano. This depth is consistent with the relatively flat elevation profile and suggests that the topography is isostatically supported by the crustal root (see Fig. 9 which shows consistency with Airy isostasy). Receiver function traces from a magnitude 7.3 Vanuatu earthquake on 2010 August 10 (Fig. 3b) show a result consistent with all other receiver function images based on multiple events. The receiver function traces show signals from the mid-crustal structure, Moho, slab and crustal multiples. Finite difference modelling based on receiver function results for Line 2 using a simplified 2-D velocity model produces synthetic receiver functions consistent with the receiver function data (Figs 3c and d). CCP stacks were done for both the *P*/*PP* and *PKP* receiver functions and the resultant images are shown in Fig. 4 which is consistent with Fig. 3(a). Although the primary slab signal observed for Line 2 is a negative impedance signal consistent with finite difference modelling results, a positive impedance signal roughly following the shape of the slab is observed above the negative slab signal as seen in Figs 3 and 4. Another check on the shape of the slab is receiver function migration using a simple homogenous velocity model for the crust. The results are shown in Fig. 5, which shows a discontinuous signal from the Moho and mid-crustal structure and a clear change from negative to positive impedance near where the top of the slab is expected. Although a weak, discontinuous Moho signal is present at depths expected from other images, inversion artefacts and other noise interference largely removes the signal in the migrated image so it is useful to compare with other imaging approaches such as CCP stacking in Fig. 4. The initial model for the expected slab location (see lines in Figs 3a and 5) is based on slab contours from the Slab 1.0 model of Hayes *et al.* (2012).

Several different models for the shape of the slab were considered and modelled using the finite difference method for comparison with the receiver function data, including a linear transition, an abrupt

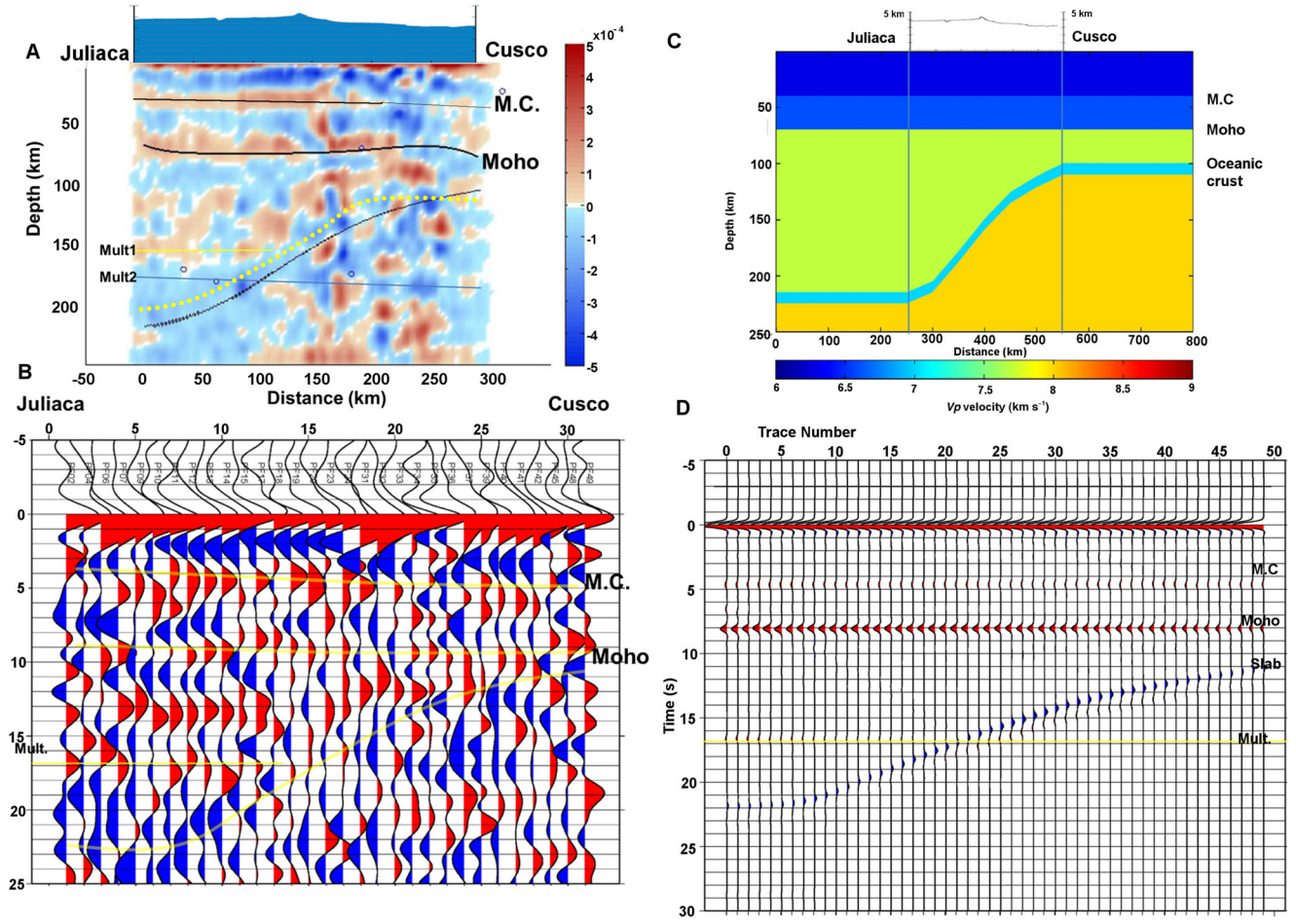

Figure 3. Results from Line 2 showing the transition from normal subduction in the southernmost part of Peru near Juliaca to shallow or flat slab subduction to the north near Cusco. (a) Receiver function image for Line 2 based on stacks of *P* and *PP* receiver functions for each station. Distance from Juliaca in kilometres is plotted against depth in kilometres. The black lines show a positive impedance mid-crustal structure at around 40 km depth, the Moho at around 70–75 km depth and the shape of the slab which is delineated primarily by a negative impedance signal. Also observable is a positive impedance arrival above the negative slab signal which also appears to be related to the slab. The positive pulse can be compared to the positive slab arrival for Line 1 in Fig. 12(b). The solid line showing expected location for the slab is based on slab contours and fits to seismicity (Slab 1.0 model, Hayes *et al.* 2012). The dotted yellow line shows an observed negative receiver function pulse that follows the expected path of the slab. (b) The receiver function plot below shows receiver functions from a magnitude 7.3 earthquake occurring near Vanuatu Islands on 2010 August 10. (c) Simple 2-D *P*-wave velocity model used for finite difference modelling based on receiver function results. (d) Synthetic receiver functions from finite difference model showing *P*-wave arrival, mid-crustal structure, Moho, slab and multiple arrival.

transition consistent with a slab break and a gently bending model shown in Fig. 3 (see Supporting Information for alternative models). The receiver function results such as Fig. 4 best match the bending model.

The Moho and *Vp*/*Vs* results obtained from receiver function stacking using the method of Zhu & Kanamori (2000) are summarized in Fig. 8, which shows station elevation, Moho depths and *Vp*/*Vs* ratios. The Moho is relatively flat for Line 2 and increases with depth to a maximum depth of 75 km near Line 3 with a decrease in crustal thickness notable where station elevation begins to decrease.

3.2 Line 3 results: flat slab region

The third seismic array runs from the coast near Nazca northeast to Cusco in the region of shallow subduction just south of where the continuation of the Nazca Ridge is subducting. The shallow slab can be clearly seen to a depth of about 100 km in Fig. 6, as well as the Moho at an average depth of 70–75 km. A mid-crustal structure is observed as well (see Fig. 7a for clarification). The receiver function traces from the NW backazimuth in Fig. 7b also show the Moho signal clearly as well as the signal from the slab as it flattens at 100 km depth. A more complete image showing that the slab remains flat for the extent of the array can be seen in the CCP stacks plotted in Fig. 6(b). The receiver function results can be compared to 2-D finite-difference models as in Fig. 7(a). The model that fits the data best includes a velocity increase between the upper and lower crust. The synthetic receiver functions show a double pulse structure the full length of the subducting oceanic crust, which is consistent with Fig. 6(b), which includes receiver function data from all azimuths while in single azimuth images such as Fig. 6(a) the positive impedance signal from the base of the oceanic crust is more difficult to detect at greater distances and depths.

Moho depths for Line 3 in Fig. 8 indicate isostatic compensation under much of the Altiplano but the fit to Airy isostasy is not as good near the coast where the slab depth is shallower,

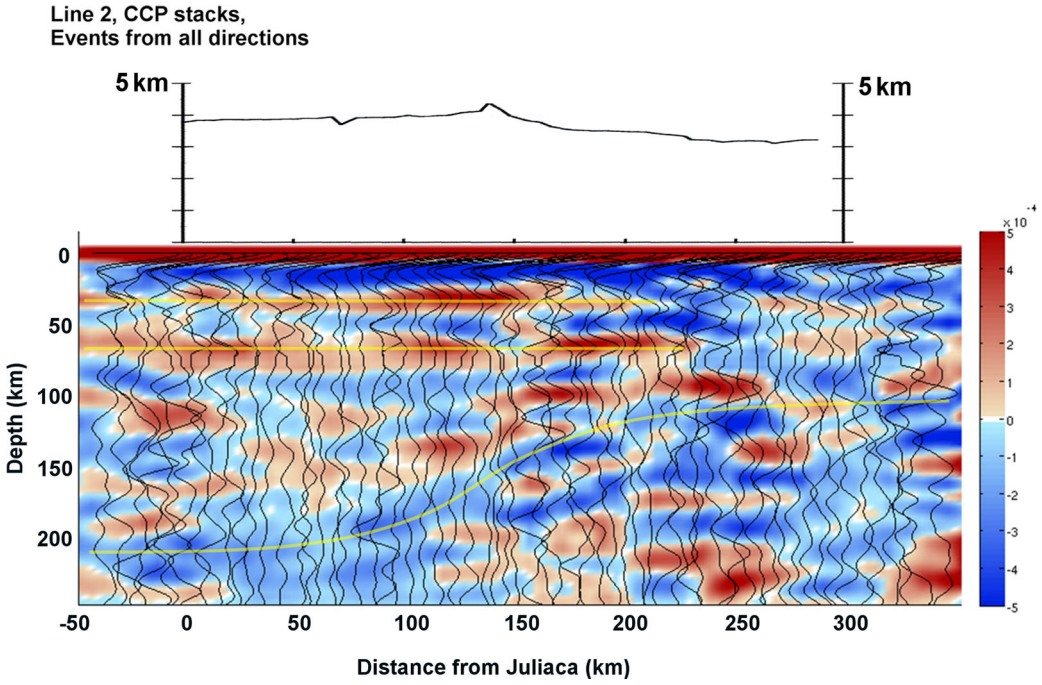

Figure 4. Plot of common conversion point (CCP) stacks with bin spacing equal to station spacing. The stack traces are shown overlying the amplitude of the stack with some horizontal smoothing. Receiver functions included in the stacks come from all azimuthal directions. The images show the mid-crustal structure, Moho signal (positive impedance signals) which are both relatively flat and the slab signal which is observed as a negative impedance signal underlying a positive slab arrival. The station elevation is shown above the image (note the different scale from the CCP image).

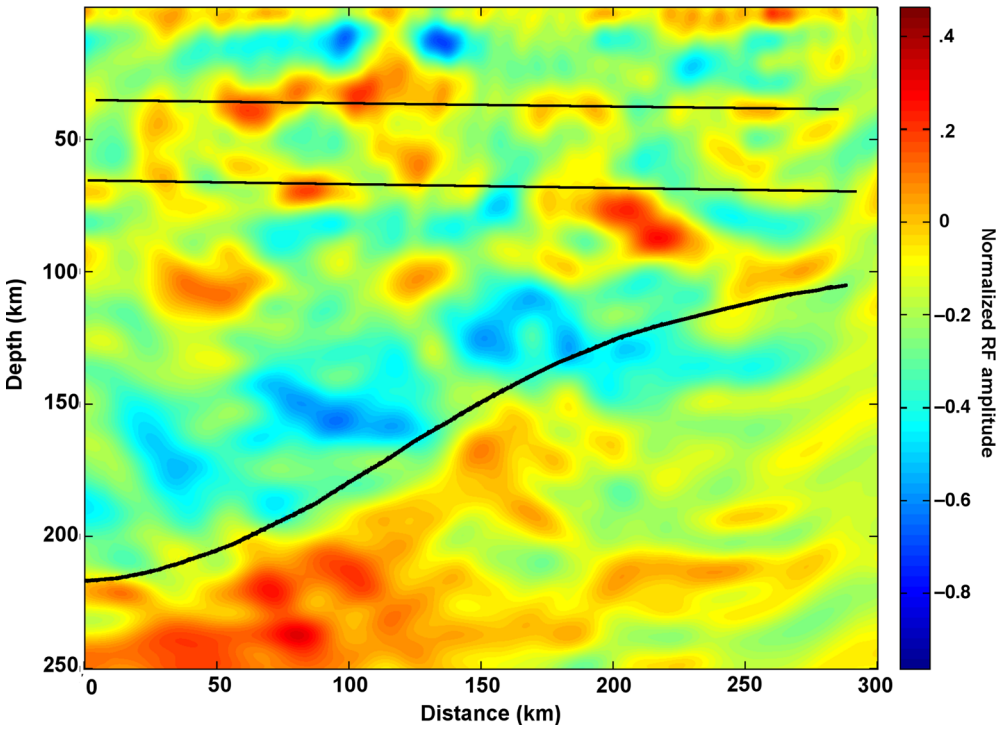

Figure 5. Line 2 receiver function migration plotted as distance from Juliaca on the *x*-axis and depth on the *y*-axis. Black lines show an interpretation of the image showing the expected location of the mid-crustal structure, Moho and slab. The location of the slab, as noted in Fig. 3(a), is based on slab contours which were then compared against the RF results. Note the change from negative to positive receiver function impedance corresponding with the expected location of the slab.

possibly as a consequence of the presence of the Nazca Ridge. The crust appears compensated within the uncertainty of the data if buoyant material is present near the coast with dimensions comparable to that of the Nazca Ridge (see Fig. 8d). The *Vp*/*Vs* ratio varies with most values falling between 1.7 and 1.8 with an average value of 1.75 and shows no strong trends other than an overall slight increase in *Vp*/*Vs* with distance from the coast.

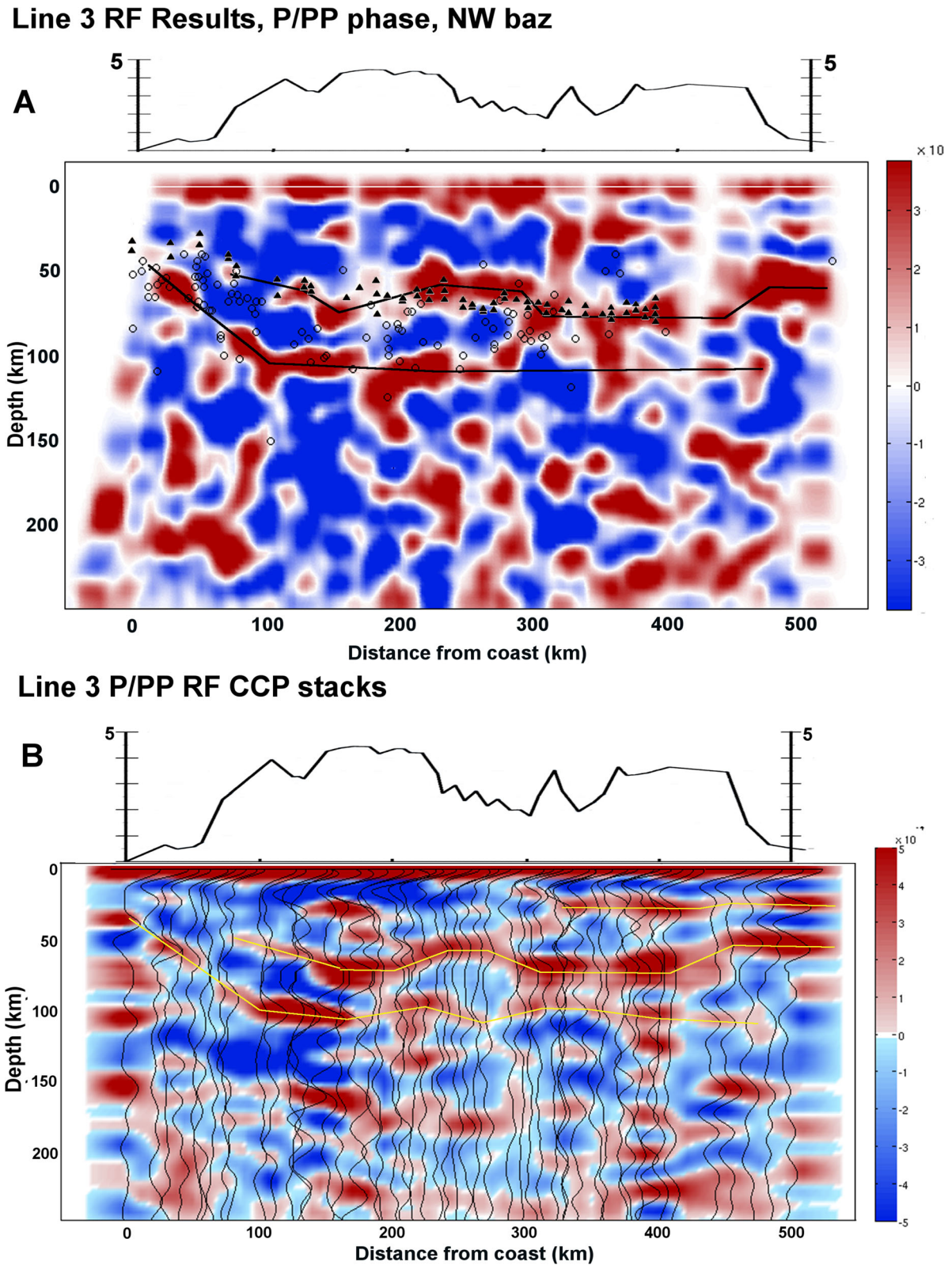

Figure 6. (a) Receiver function image for Line 3 based on *P* and *PP* receiver functions from an NW azimuth from Peru. The image was formed by backprojecting the rays from the direction in which the energy originated. Distance is from the coast near Nazca to Cusco. Open circles show hypocentral locations from NEIC. Black lines show an interpretation of the Moho with individual station picks from stacking shown as green triangles, and interpretations of the slab and mid-crustal structure. The slab can be seen flattening out at 100 km depth with the Moho just above it at around 70 km depth. Note a shallowing of Moho depth between about 200 and 300 km distance and near 500 km distance where topography decreases in elevation, indicating a good correspondence between topography and Moho depth. (b) CCP plot for Line 3 showing the stacks with background colours showing amplitude. The mid-crustal structure, Moho and slab interpretations are delineated with yellow lines.

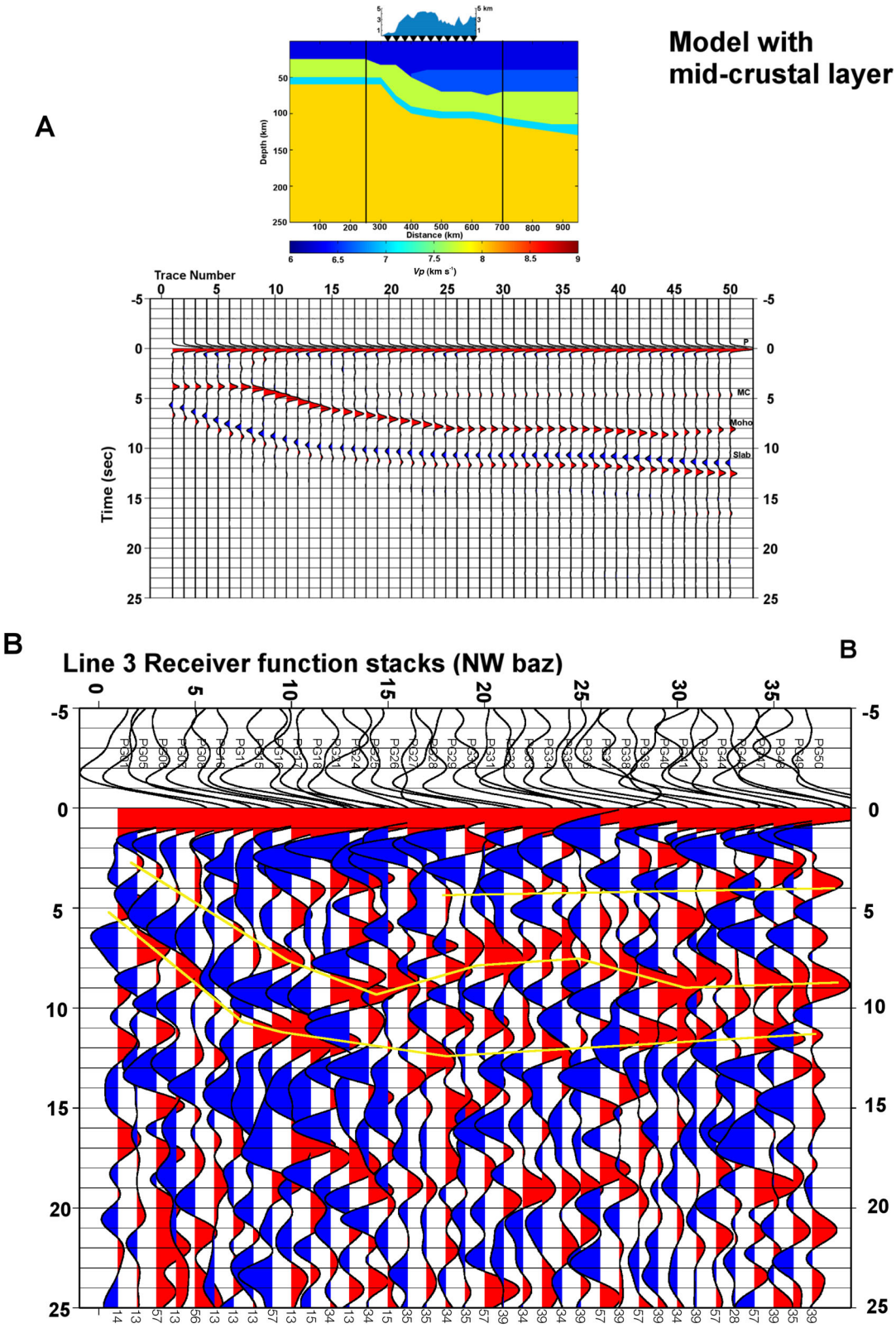

Figure 7. (a) Finite difference modelling for Line 3. The model includes a mid-crustal velocity increase. Synthetic receiver functions are consistent with receiver function results showing the double pulse structure of the slab, the positive Moho signal and mid-crustal structure. (b) Receiver function plot showing stacks for each station based on events from the northwest consistent with the images in Fig. 6. Major arrivals such as the slab signal, Moho depth and mid-crustal structure are marked by yellow lines and can be compared to the synthetics in part (a).

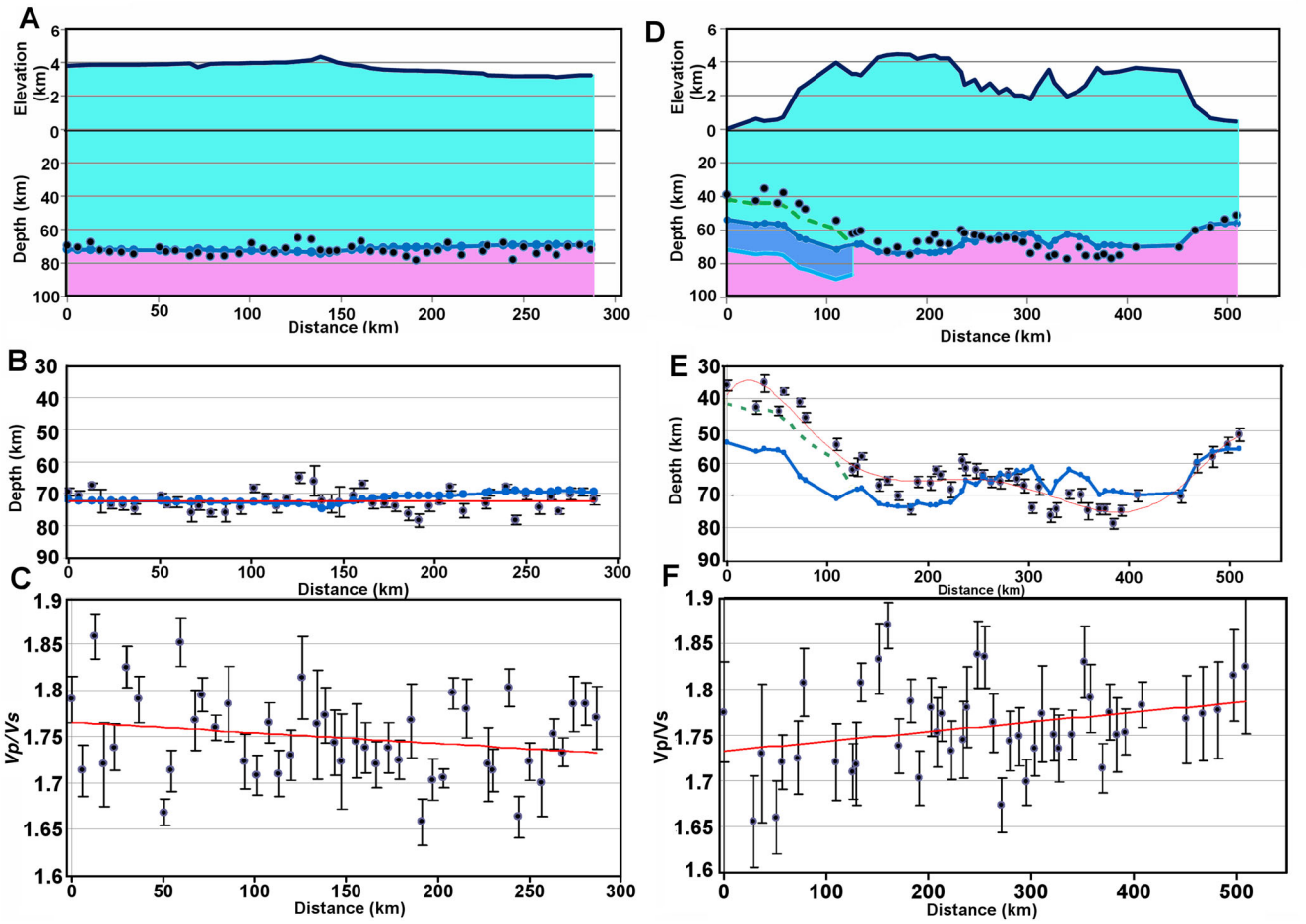

Figure 8. Moho and *Vp*/*Vs* results for Lines 2 and 3. (a) Isostasy model for Line 2 including station elevation. Note the differing scales between elevation and Moho depth. The blue line is a calculation of expected depth for Airy isostasy relative to a reference station assuming an average crustal density of 2.7 g cc^{-1} and average mantle density of 3.3 g cc^{-1}. (b) Line 2 Moho depth from stacking. The red line shows a linear fit to the data. The blue line shows the Moho depth that would be expected for Airy isostatically compensated topography. (c) Line 2 *Vp*/*Vs* ratio estimates from stacking with a red line showing linear least-squares regression. Most of the *Vp*/*Vs* values are in the average range around 1.75. (d) Line 3 isostatic model including elevation (note scales for elevation and Moho depth). The blue line shows a calculation for airy isostasy assuming the same average densities as in (a). The fit to the data is not as good near the coast unless we include additional buoyant material from the subducting oceanic crust. The crust could be expected to be slightly thicker than normal oceanic crust due to the proximity of the Nazca Ridge which is expected to have a crustal thickness of 18 km (Hampel 2002). The effect of this addition on the isostasy is noted by the green dashed line which is a better match to the data. (e) Line 3 Moho depth with a red line showing a polynomial regression curve to the data points. The blue line shows isostatic compensation depth and the green dashed line shows the correction for subducting oceanic crust. (f) Line 3 *Vp*/*Vs* ratio showing a linear regression curve to the data. There appears to be a general trend from lower *Vp*/*Vs* values near the coast to higher values near Cusco.

4 DISCUSSION

4.1 Moho depth and *Vp*/*Vs*

The maximum Moho depth of 75 km beneath the Altiplano is consistent with results for the first seismic array (Line 1) in the region of normal subduction dip (Phillips *et al.* 2012). Previous studies in the central Andes have resulted in comparable estimates for crustal thickness. Most estimates have an average value of 70 km with ranges between 59 and 80 km for crustal thickness beneath the Western and Eastern Cordilleras and Altiplano (Cunningham & Roecker 1986; Zandt *et al.* 1994; Beck *et al.* 1996; Myers *et al.* 1998; Baumont *et al.* 2001; Beck & Zandt 2002; Yuan *et al.* 2002; McGlashan *et al.* 2008; Lloyd *et al.* 2010). The crust in the Altiplano region is isostatically compensated primarily through crustal thickening (Whitman *et al.* 1993), and crustal shortening due to compression generated by plate coupling or through the Arica bend provides a significant mechanism for contributing the crustal thickness. Gotberg *et al.* (2010) show that 70 km of thickness in to the Andes would require 240–300 km of shortening but their preferred shortening estimate left a significant proportion of this shortening budget unaccounted for. Other possible mechanisms which would contribute to thickening include processes such as shortening related to the Arica bend (Kley & Monaldi 1998; Gotberg *et al.* 2010), magmatic additions or shortening hidden by the volcanic arc (Gotberg *et al.* 2010), thermal weakening, upper-mantle hydration (Allmendinger *et al.* 1997) or other factors. Another possible mechanism which would help to explain crustal thickness not accounted for by shortening, is tectonic underthrusting which would be consistent with the idea that the mid-crustal structure observed at 40 km depth is a result of underthrusting of the Brazilian shield (Whitman *et al.* 1993). In this case, the mid-crustal structure could represent the top of the Brazilian shield in which much of the overlying sediment has been eroded off and incorporated into the fold and thrust belt leaving mostly basement rock remaining. A thin layer of remaining sediment may show up as a low-velocity layer, which has been

observed in initial surface wave studies. The positive impedance signal at about 40 km depth is observed strongly across Line 2 and also is seen in the easternmost portions of the two arrays perpendicular to the trench. The possible correlation between the signal at 40 km depth with the underthrusting of the Brazilian shield is discussed in Phillips *et al.* 2012. This mechanism is more consistent with a gradual uplift model for this part of the Altiplano (Elger *et al.* 2005; McQuarrie *et al.* 2005; Oncken *et al.* 2006; Barnes & Ehlers 2009; Ehlers & Poulsen 2009). Further discussion of crustal thickness and properties and implications for possible underthrusting of the Brazilian shield can be found in Phillips *et al.* 2012.

Vp/*Vs* ratios appear to have an average value between 1.73 and 1.75 with few discernible patterns in terms of areas of higher or lower *Vp*/*Vs*. A *Vp*/*Vs* ratio of 1.73–1.75 corresponds to a Poisson's ratio of 0.25 to 0.26, which is compatible with previous results for the Altiplano (Zandt & Ammon 1995; Beck *et al.* 1996; Swenson *et al.* 2000). The observed values of the *Vp*/*Vs* ratio support the conclusion that the crust in the transition and flat slab region does not have a high degree of partial melting, consistent with the observed volcanic gap, since there are no regions with abnormally high values as might be expected where a magma body is present. The location of the active volcanic arc relative to the arrays can be seen in Fig. 1 which confirms that Lines 2 and 3 are located outside of the volcanic region. *Vp*/*Vs* results for Line 1 in the region of normal subduction showed a few areas of higher *Vp*/*Vs* values near the active volcanic arc, which may be indicative of magmatism (Phillips *et al.* 2012). The amount of variation in *Vp*/*Vs* measurements is partly due to uncertainty in cases where the multiples on which they rely are not readily apparent in the receiver function data resulting in less constraint on *Vp*/*Vs* results. An example is seen in the Supporting Information where the signal from the Moho is observed more clearly than the multiple arrivals. The uncertainty is given by the 95 per cent contour line and gives a 1σ value of about 0.035 which is an average uncertainty estimate for error due to sources such as noise and unclear multiple arrivals.

4.2 Slab structure

The shape of the slab is delineated through various images from different backazimuths and the use of both *P*/*PP* and *PKP* receiver functions. For Line 2, the transition from normal to flat slab subduction, the slab signal appears as a primarily negative impedance signal (see Figs 3–5), which agrees with the finite difference modelling results. The transition from normal ($\sim 30^\circ$) subduction near Juliaca to flat slab subduction near Cusco appears to be gradual, thus there is no evidence that the subducting Nazca Ridge caused a break in the slab. A subduction transition, which appears as a smooth bend in the slab is consistent with previous seismicity studies such as Hasegawa & Sacks (1981), Grange *et al.* (1984) and Schneider & Sacks (1987). If the slab was tearing we would expect to see observe evidence of tearing also to the north as the Nazca Ridge propagated down the coast, and there is no evidence for this. Note that the point where the slab is starting to flatten is some 400 km ahead to the projection of the Nazca Ridge. There is no indication in the seismicity that the slab returns to normal dip after the passage of the Nazca Ridge. Note the contrast with central Chile where the uplift is 130 km ahead of the projection of the Juan Fernandez Ridge and returns to its original dip within 150 km in its wake (estimated from slab contours, see Anderson *et al.* 2007).

In addition to the observed slab structure for the transition region of Line 2, a strong signal from the slab was also observed in the receiver function images for Line 3 located in the flat slab region. In contrast to the negative impedance slab signal from the transition region, a positive impedance signal can be seen for the flat slab region in Figs 6 and 7. The strongest amplitude of the double pulse slab structure can be seen in the first $\sim$250 km of distance from the trench as the slab is descending to a depth of 100 km. This may be a result of the deeper subduction of hydrated oceanic sediments prior to dehydration of the minerals in the crust at greater distances and depths (Katayama *et al.* 2006; Kawakatsu & Watada 2007). The slab shape from receiver function depths can be seen in comparison with the Slab 1.0 model for all of the arrays in Fig. 9. A comparison of the models for the normal, transition and flat slab regions and corresponding synthetic receiver functions can be seen in Fig. 10, which has similar velocities for all three 2-D models. For the three different 2-D models with shapes representative of the three different subduction regimes, the finite difference runs were performed with similar ray parameters and slab orientations (shallowest part of slab on left) such that the only difference is the shape of the slab, which impacts the transmission angle of the incoming energy. Note that the observed slab signal in the synthetic receiver functions differs for different slab shapes, with a dominantly negative impedance signal in the transition region, a double pulse signal in the flat slab region and a double pulse signal for the shallower part of the normal subduction region. The effect of the angle of incidence on the observed slab signal in receiver functions was also investigated by varying the ray parameter and location from which the plane wave originates in finite difference simulations. Such simulations showed that it was even possible to get a positive pulse overlying a negative pulse for certain steep angles of incidence. This was also noted in Phillips *et al.* (2012) particularly with respect to *PKP* receiver functions which arrive at a very steep angle and produce a slab signal that was inverted with respect to that of *P*/*PP* receiver functions. Thus the reason why the slab signal appears to be mainly a negative impedance signal for Line 2 (see Figs 3c and d) compared to the slab signals for the other two arrays appears to be related to the subduction zone structure and angle of the subducted oceanic crust and a change in the transmission coefficient for certain angles of incidence.

4.3 Nazca Ridge and causes of flat slab subduction

The Nazca Ridge is currently subducting at a latitude of -15°S and has a projection that puts the portion of the ridge that has already subducted just north of Line 3 (see Fig. 1). The Nazca Ridge has a trend of N42°E at a region where the convergence direction is 77° resulting in an oblique angle of subduction and southward ridge migration (Hampel 2002). According to Hampel (2002), the Nazca Ridge began subducting at 11°S at 11.2 Ma and is presently migrating at 43 mm a^{-1}. Several authors have considered the buoyancy effect of the Nazca Ridge as a mechanism to support the development of flat slab subduction (Gutscher *et al.* 1999a, 200b; van Hunen *et al.* 2002a,b). The ridge is a wide feature (200 km wide, 1.5 km high, with a total crustal thickness of 17 km) so the stations on the array closest to the coast are most likely to show the impact of the subducting ridge on the subduction system. Some of the expected effects of the subducting ridge on the coastal region are deformation of the upper plate, uplift in the forearc, westward shift of the coastline (Hampel 2002) and a gravity anomaly corresponding to the crustal root supporting the ridge (Macharé & Ortlieb 1992; Hampel *et al.* 2004). The coastal stations show possible evidence

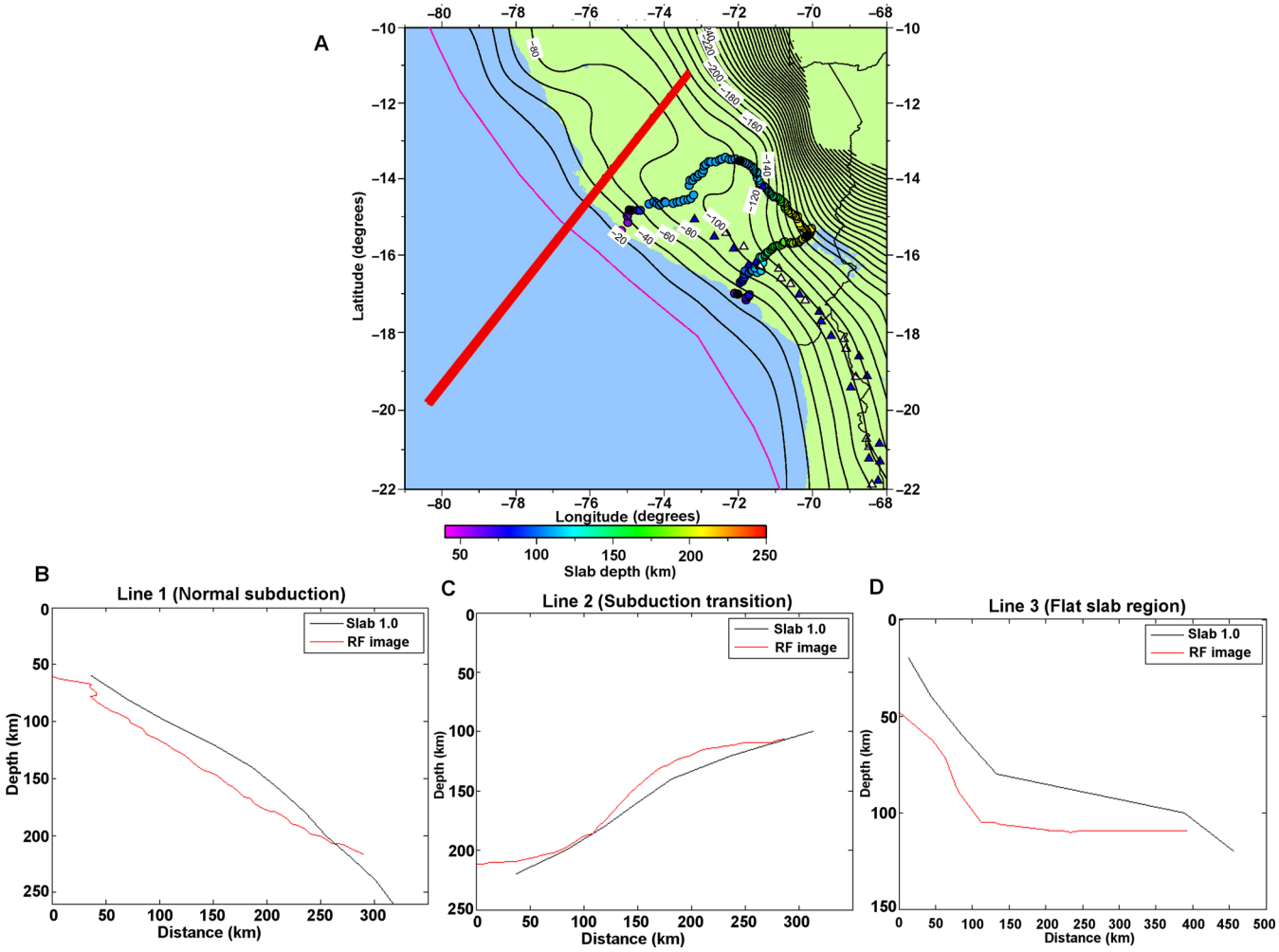

Figure 9. Comparison of Slab 1.0 contours with slab depths obtained from receiver functions and the expected location of the Nazca Ridge (shown by the red line). Part (a) shows the depths in map view and (b)–(d) show estimates in 2-D of the comparison based on graphical digitalizations of receiver function images. Within the uncertainty of the depth estimates, the receiver function depth estimates are observed to be comparable to the Slab 1.0 model based on seismicity, although for Line 3 the receiver function observations put the slab depth at a slightly greater depth. The slab signal is observed at about 100 km depth after a distance of ∼100 km from the coast.

of some uplift in the forearc compared to the normal subduction region but overall the elevation profiles are similar (see Fig. 12a).

A comparison of receiver function results from Line 3 near the subducting Nazca Ridge with results from the region of normal subduction further south between Mollendo and Juliaca can be seen in Fig. 11. The slab dips near the trench are initially similar before the flat slab quickly flattens out at 100 km while in the normal region the slab continues descending at a constant angle. The Moho in both cases is relatively flat at a depth of around 70 km for much of the central section of the Altiplano. One notable difference between the Moho in the flat and normal subduction regions is that the positive impedance signal from the Moho is less distinct for the flat slab region (Line 3) near the coastline where the slab is descending from the trench while for the normal subduction region (Line 1) the Moho is clear throughout the whole range of the array. The reason for this may be that the flat slab region has a cooler thermal structure and less slab dehydration, which could change the wedge velocity such that it has no contrast with the crust (Bostock *et al.* 2002). Another difference between the Moho observed in the two regions is that in the case of the flat slab, there is a narrower gap of only about 30 km between the Moho at 70 km depth and top of the slab at 100 km depth so there is no room for asthenospheric material, which provides an explanation for the observed volcanic gap observed in the flat slab region. A thin mantle lithosphere is expected between the continental Moho and subducting plate. The difference between Moho depth and the subducting plate impacts the degree of coupling between the Nazca Plate and overriding South American Plate and thus the degree of intraplate hydrostatic suction which has been proposed as a possible factor in encouraging flat slab subduction.

A comparison of the topography in the forearc region to the Western Cordillera for both the normal and flat slab regions can be seen in Fig. 12(a). Although there are similarities in the overall rise, Line 1 is almost flat for the first 30 km before showing a sudden jump to an elevation of about 1.2 km while Line 3 initially rises more rapidly before flattening out until 60 km from the coast. Thus, at a distance of 30 km from the coast, Line 3 has an elevation about 400 m higher than Line 1 has at the same distance from the trench. This may correspond to the several hundred metres of forearc uplift mentioned by Hampel (2002) as resulting from the subduction of the Nazca Ridge.

In addition to comparing the topography, Figs 12(b)–(d) show a comparison of the seismicity between the flat slab and normal

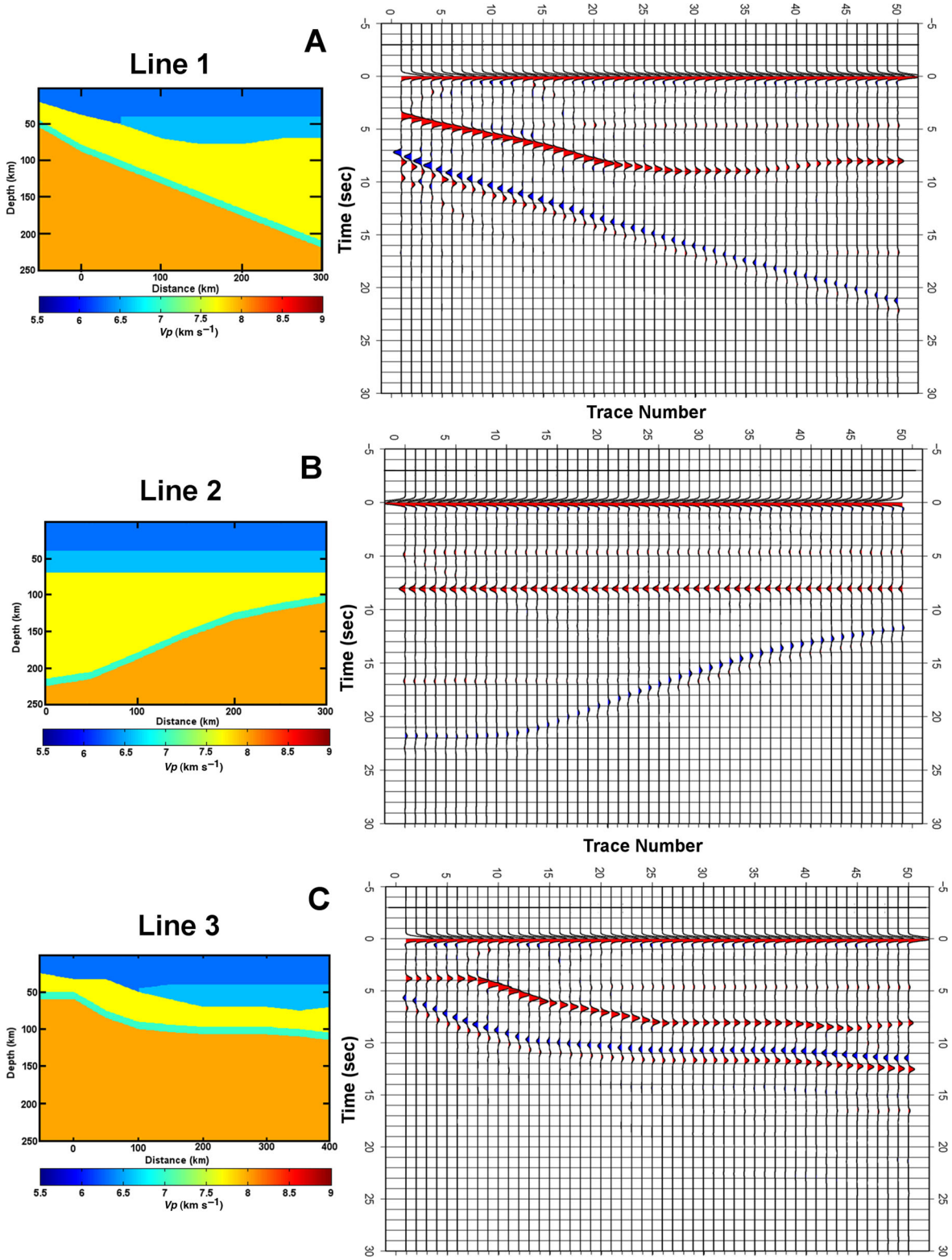

Figure 10. Comparison of synthetic models for all three seismic arrays showing (a) the region of normal subduction (Line 1), (b) the transition from normal to flat slab subduction (Line 2) and (c) flat slab region (Line 3). Note that the synthetic receiver functions for Line 3 show a double pulse slab signal while the slab for Line 1 is double pulse mainly for the upper half and primarily negative at depth while the slab signal for Line 2 is mostly a negative impedance signal.

subduction region both in terms of seismicity in the Wadati–Benioff zone defining the shape of the slab and crustal seismicity, which provides some measure of amount of faulting and deformation in the upper plate. The seismicity comes from the National Earthquake Information Center (NEIC) catalogue for the past 30 yr (1982–2012) including events larger than *M*w 4.0. Events were removed in which the depths were not well defined and were given a default crustal depth of 33 km. The overall number of events is greater in the south

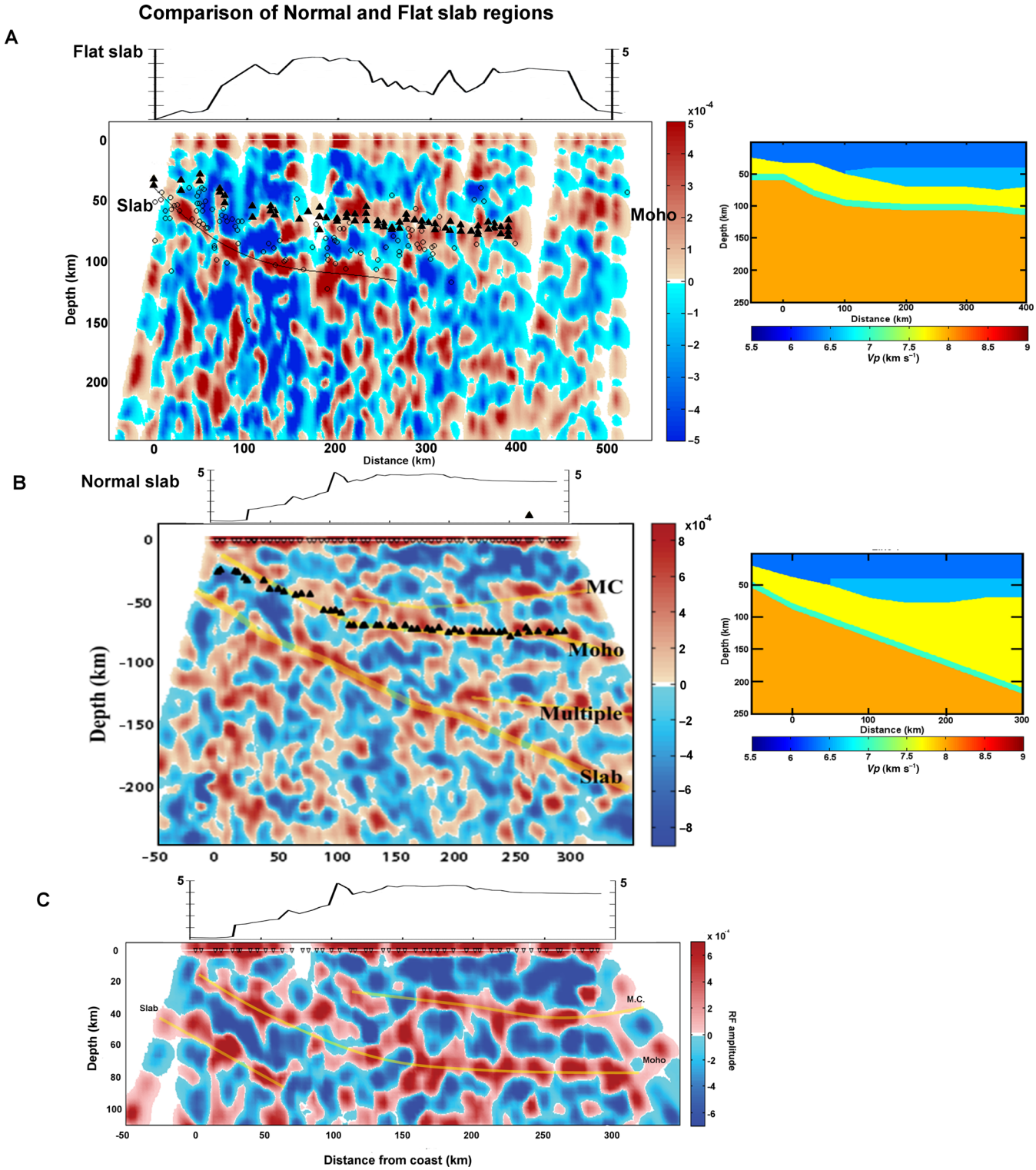

Figure 11. Comparison of the structure of the normal subduction region (Line 1) and flat slab region (Line 3). (a) Line 3 from Nazca to Cusco. Moho picks from stacking are shown by green triangles. (b) Results from Line 1 in the normal subduction region showing the 30° dipping slab using *P*/*PP* receiver functions from an NW backazimuth. Note that the double pulse slab signal from Line 3 (a) is most clear up to 100 km before appearing as a primarily negative signal while the slab in the region of normal subduction is seen as a positive impedance signal at all depths down to a depth of about 200 km. Simple models of the normal and flat slab regions used for finite difference modelling are shown to the right of the images. (c) An image from Line 2 using *P*/*PP* receiver functions from all azimuthal directions showing only the upper 120 km. The Moho can be clearly seen as can a mid-crustal structure at 40 km depth which is suggested to be from underthrusting of the Brazilian shield.

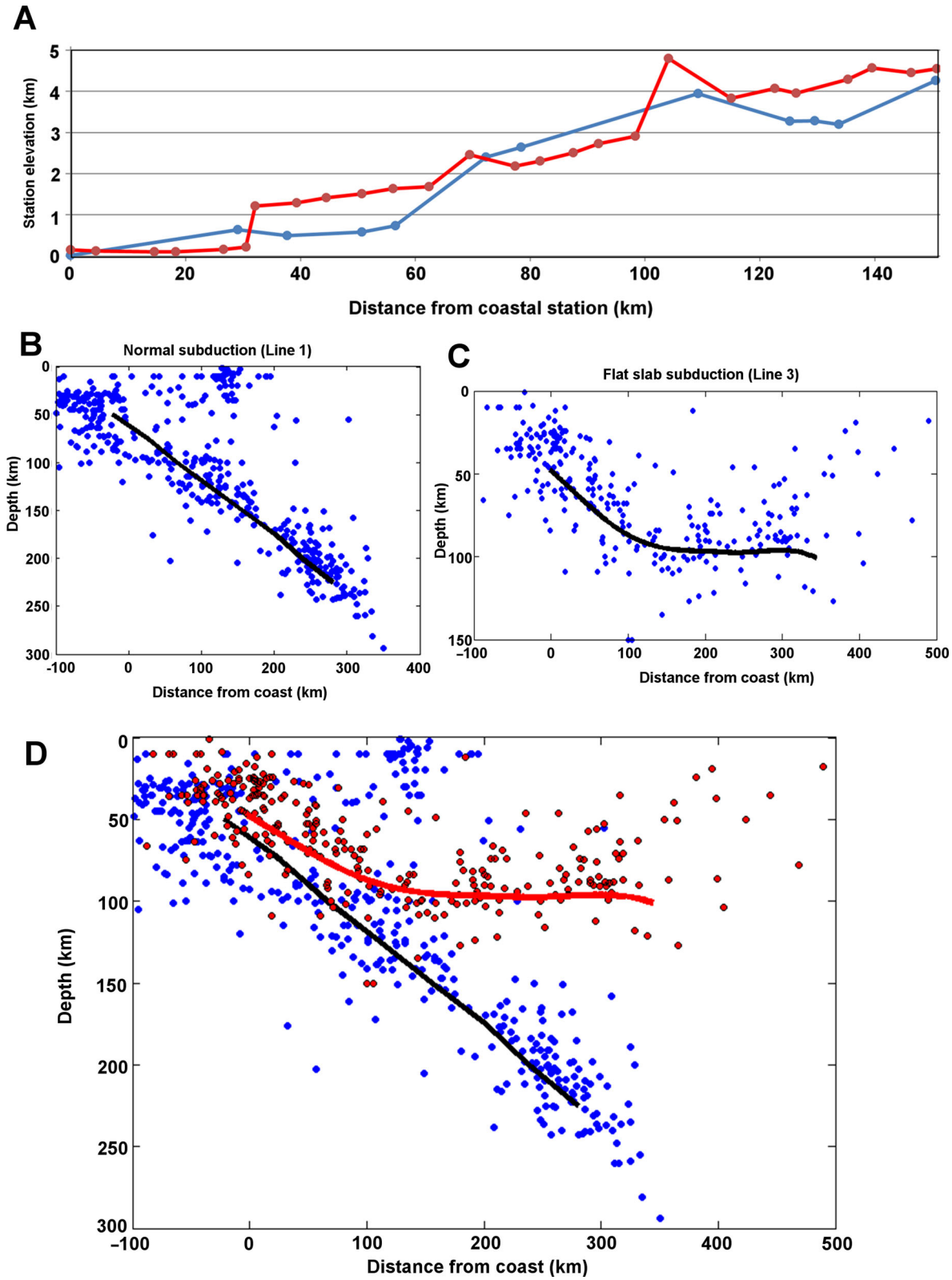

Figure 12. (a) Comparison of station elevation for Line 1 (normal subduction) shown by the red line with elevation of Line 3 (flat slab subduction) shown by the blue line. (b) Depth versus distance seismicity cross-section for Line 1 where the black line represents the approximate location for the top of subducting Nazca Plate. Earthquakes are from the NEIC catalogue from 1982 to 2012 for events of magnitude greater than 4.0. (c) Same as in (b) but for Line 3 in the flat slab region. (d) Overlay of the plots shown in parts (b) and (c) to allow for comparison of the flat slab and normal subduction region.

where normal subduction is occurring. The difference in level of crustal seismicity does not appear to be significant although in the case of normal subduction there appears to be a cluster of events near the centre of the array at a very shallow depth, which is likely related to activity near the active volcanic arc.

In terms of a cause of flat slab subduction, most authors conclude that the Nazca Ridge does not have sufficient buoyancy by itself to sufficiently support the length of the Peruvian flat slab (Gutscher *et al.* 1999a,b; van Hunen *et al.* 2002a, 2004). Other factors present in Peru which can impact dip angle are the fast subduction velocity relative to the motion of the overriding plate, intermediate age of subducting lithosphere (30–40 Ma), the Arica bend, hydrostatic suction and possibly cycles of repeated slab breakoff and flat slab subduction since repeated flat subduction events through time have been documented in the Andes (Haschke *et al.* 2007). Although the main cause and relative importance of various causes are outside the scope of the data collected in this study, we conclude that the motion of the Nazca Ridge sweeping down the coast is unlikely to be a significant cause of flat slab subduction. The length of flat slab segment south of the Nazca Ridge appears too long to be supported by buoyancy of the ridge alone and regions north of the ridge do not return to normal dip after the ridge has passed.

5 CONCLUSIONS

Receiver function studies from seismic arrays in southern Peru provide more details of the structure of the transition region from normal (30° dip) subduction to flat slab subduction. The Moho beneath the Altiplano is found to have a maximum depth of 75 km. The depth of the Moho is found to be consistently deep beneath the Altiplano beneath southern Peru. The Moho is observed to be almost flat at an average depth of 70 km underneath the north–south trending array, which contrasts with other areas of South America where more topography of the Moho is observed. The shape of the slab is also clarified and the transition is found to be gradual from normal to flat slab subduction, which indicates that the change is most likely a contortion rather than a break in the slab. The slab is observed have an almost constant depth of 100 km beneath the array in the flat slab region. The observed impacts of the Nazca Ridge and flat slab subduction from this study are a lessening of overall seismicity, minor uplift in the forearc region and a less defined Moho transition near the coast.

ACKNOWLEDGEMENTS

We thank the Betty and Gordon Moore Foundation for their support through the Tectonics Observatory at Caltech. This research was partially support by NSF award EAR-1045683. Also thanks to Richard Guy, Paul Davis and Igor Stubailo of the UCLA Center for Embedded Networked Systems, Steven Skinner of the Caltech Seismological Laboratory, Hernando Tavera and Victor Aguilar of the Instituto Geofisico del Peru and Laurence Audin of Institute of Research for Development. We also thank the PULSE and CAUGHT projects for contributing data to this study. Contribution #238 from the Tectonics Observatory.

REFERENCES

Abers, G., 2000. Hydrated subducted crust at 100–250 km depth, *Earth planet. Sci. Lett.,* **176,** 323–330.

Abers, G., van Keken, P., Kneller, E., Ferris, A. & Stachnik, J., 2006. The thermal structure of subduction zones constrained by seismic imaging: implications for slab dehydration and wedge flow, *Earth planet. Sci. Lett.,* **241,** 387–397.

Allmendinger, R., Jordan, T., Kay, S. & Isacks, B., 1997. The evolution of the Altiplano-Puna plateau of the Central Andes, *Annu. Rev. Earth planet. Sci.,* **25,** 139–174.

Ammon, C., 1991. The isolation of receiver effects from teleseismic P waveforms, *Bull. seism. Soc. Am.,* **81**(6), 2504–2510.

Anderson, M., Alvarado, P., Zandt, G. & Beck, S., 2007. Geometry and brittle deformation of the subducting Nazca Plate, central Chile and Argentina, *Geophys. J. Int.,* **171,** 419–434.

Barazangi, M. & Isacks, B.L., 1976. Spatial distribution of earthquakes and subduction of the Nazca plate beneath South America, *Geology,* **4,** 686–692.

Barnes, J. & Ehlers, T., 2009. End member models for Andean Plateau uplift, *Earth Sci. Rev.,* **97,** 105–132.

Baumont, D., Paul, A., Zandt, G. & Beck, S.L., 2001. Inversion of Pn travel times for lateral variations of Moho geometry beneath the central Andes and comparison with the receiver functions, *Geophys. Res. Lett.,* **28**(9), 1663–1666.

Beate, B., Monzier, M., Spikings, R., Cotton, J., Silva Bourdon, J.E. & Eissen, J., 2001. Mio-Pliocene adakite generation related to flat subduction in southern Ecuador: the Quimsacocha volcanic center, *Earth planet. Sci. Lett.,* **192,** 561–570.

Beck, S. & Zandt, G., 2002. The nature of orogenic crust in the central Andes, *J. geophys. Res.,* **107**(B10), doi:10.1029/2000JB000124.

Beck, S., Zandt, G., Myers, S., Wallace, T., Silver, P. & Drake, L., 1996. Crustal-thickness variations in the central Andes, *Geology,* **24**(5), 407–410.

Bevis, M., 1986. The curvature of Wadati-Benioff zones and the torsional rigidity of subducting plates, *Nature,* **323,** 52–53.

Bostock, M., Hyndman, R., Rondenay, S. & Peacock, S., 2002. An inverted continental Moho and serpentinization of the forearc mantle, *Nature,* **417,** 536–538.

Cahill, T. & Isacks, B.L., 1992. Seismicity and shape of the subducted Nazca Plate, *J. geophys. Res.,* **97**(B12), 17 503–17 529.

Cunningham, P. & Roecker, S., 1986. Three-dimensional P and S wave velocity structures of southern Peru and their tectonic implications, *J. geophys. Res.,* **91**(B9), 9517–9532.

Dorbath, C., Gerbault, M., Carlier, G. & Guiraud, M., 2008. Double seismic zone of the Nazca plate in northern Chile: high-resolution velocity structure, petrological implications, and thermo-mechanical modeling, *Geochem. Geophys. Geosyst.,* **9**(7), Q07006, doi:10.1029/2008GC002020.

Eakin, C.M., Long, M.D, Beck, S.L. & Wagner, L.S., 2011. Seismic anisotropy and mantle flow beneath the Peruvian flat slab region, in *AGU, Fall Meeting 2011,* abstract #DI44B-04.

Ehlers, T. & Poulsen, C., 2009. Influence of Andean uplift on climate and paleoaltimetry estimates, *Earth planet. Sci. Lett.,* **281,** 238–248.

Elger, K., Oncken, O. & Glodny, J., 2005. Plateau-style accumulation of deformation: southern Altiplano, *Tectonics,* **24,** TC4020, doi:10.1029/2004TC001675.

Engdahl, E.R. & Villaseñor, A., 2002. Global seismicity: 1900–1999, in *International Handbook of Earthquake and Engineering Seismology,* Part A, Chapter 41, pp. 665–690, eds Lee, W.H.K., Kanamori, H., Jennings, P.C. & Kisslinger, C., Academic Press.

Gotberg, N., McQuarrie, N. & Caillaux, V., 2010. Comparison of crustal thickening budget and shortening estimates in southern Peru (12–14 S): implications for mass balance and rotations in the 'Bolivian orocline', *Bull. geol. Soc. Am.,* **122**(5–6), 727–742.

Grange, F. *et al.*, 1984. The configuration of the seismic zone and the downgoing slab in southern Peru, *Geophys. Res. Lett.,* **11**(1), 38–41.

Gutscher, M., Olivet, J., Aslanian, D., Eissen, J. & Maury, R., 1999a. The 'lost Inca Plateau': cause of flat subduction beneath Peru? *Earth planet. Sci. Lett.,* **171**(3), 335–341.

Gutscher, M., Malavielle, J., Lallemand, S. & Collot, J., 1999b. Tectonic segmentation of the North Andean margin: impact of the Carnegie Ridge collision, *Earth planet. Sci. Lett.,* **168,** 255–270.

Gutscher, M., Maury, R., Eissen, J. & Bourdon, E., 2000a. Can slab melting be caused by flat subduction? *Geology,* **28**(5), 535–538.

Gutscher, M., Spakman, W., Bijwaard, H. & Engdahl, E., 2000b. Geodynamics of flat subduction: seismicity and tomographic constraints from the Andean margin, *Tectonics,* **19**(5), 814–833.

Hampel, A., 2002. The migration history of the Nazca Ridge along the Peruvian active margin: a re-evaluation, *Earth planet. Sci. Lett.,* **203,** 665–679.

Hampel, A., Kukowski, N., Bialas, J., Huebscher, C. & Heinbockel, R., 2004. Ridge subduction at an erosive margin: the collision zone of the Nazca Ridge in southern Peru, *J. geophys. Res.,* **109,** B02101, doi:10.1029/2003JB002593.

Haschke, M., Gunther, A., Melnick, D., Echtler, H., Reutter, K., Scheuber, E. & Onken, O., 2007. Central and southern Andean tectonic evolution inferred from arc magmatism, in *The Andes: Active Subduction Orogeny*, Frontiers Earth Science, Chap. 16, Vol. 1, pp. 337–354, eds Oncken, O., Chong, G., Franz, G., Giese, P., Götze, H.-J., Ramos, V.A., Strecker, M.R. & Wigger, P., Springer.

Haschke, M.R., Scheuber, E., Gunther, A. & Reutter, K., 2002. Evolutionary cycles during the Andean orogeny: repeated slab breakoff and flat subduction? *TerraNova,* **14**(1), 49–55.

Hasegawa, A. & Sacks, I.S., 1981. Subduction of the Nazca Plate beneath Peru as determined from seismic observations, *J. geophys. Res.,* **86**(136), 4971–4980.

Hayes, G.P., Wald, D.J. & Johnson, R.L., 2012. Slab1.0: a three-dimensional model of global subduction zone geometries, *J. geophys. Res.,* **117,** B01302, doi:10.1029/2011JB008524.

International Seismological Centre, 2010. On-line Bulletin, Available at: http://www.isc.ac.uk (last accessed 18 October 2012), *Internatl.* Seis. Cent., Thatcham, United Kingdom.

Jischke, M., 1975. Dynamics of descending lithospheric plates and slip zones, *J. geophys. Res.,* **80,** 4809–4813.

Katayama, I., Nakashima, S. & Yurimoto, H., 2006. Water content in natural eclogite and implications for water transport into the deep upper mantle, *Lithos,* **86,** 245–259.

Kawakatsu, H. & Watada, S., 2007. Seismic evidence for deep-water transportation in the mantle, *Science,* **316,** 1468–1471.

Kim, Y., Clayton, R.W. & Jackson, J.M., 2010. Geometry and seismic properties of the subducting Cocos plate in central Mexico, *J. geophys. Res.,* **115,** B06310, doi:10.1029/2009JB006942.

Kley, J. & Monaldi, C.R., 1998. Tectonic shortening and crustal thickness in the Central Andes: how good is the correlation? *Geology,* **26**(8), 723–726.

Langston, C., 1979. Structure under Mount Rainier, Washington, inferred from teleseismic body waves, *J. geophys. Res.,* **84,** 4749–4762.

Ligorría, J. & Ammon, C., 1999. Iterative deconvolution and receiver function estimation, *Bull. seism. Soc. Am.,* **89**(5), 1395–1400.

Lloyd, S., van der Lee, S., Sand Franca, G., Assumpcao, M. & Feng, M., 2010. Moho map of South America from receiver functions and surface waves, *J. geophys. Res.,* **115,** B11315, doi:10.1029/2009JB006829.

Macharé, J. & Ortlieb, L., 1992. Plio-Quaternary vertical motions and the subduction of the Nazca Ridge, central coast of Peru, *Tectonophysics,* **205,** 97–108.

Manea, V., Perez-Gussinye, M. & Manea, M., 2012. Chilean flat slab subduction controlled by overriding plate thickness and trench rollback, *Geology,* **40**(1), 35–38.

McGeary, S., Nur, A. & Ben-Avraham, Z., 1985. Spatial gaps in arc volcanism: the effect of collision or subduction of oceanic plateaus, *Tectonophysics,* **119,** 195–221.

McGlashan, N., Brown, L. & Kay, S., 2008. Crustal thickness in the central Andes from teleseismically recorded depth phase precursors, *Geophys. J. Int.,* **175,** 1013–1022.

McQuarrie, N., Horton, B., Zandt, G., Beck, S. & DeCelles, P., 2005. Lithospheric evolution of the Andean fold-thrust belt, Bolivia, and the origin of the central Andean plateau, *Tectonophysics,* **399,** 15–37.

Myers, S., Beck, S., Zandt, G. & Wallace, T., 1998. Lithospheric-scale structure across the Bolivian Andes from tomographic images of velocity and attenuation for P and S waves, *J. geophys. Res.,* **103**(21), 233–221, 252.

O'Driscoll, L., Richards, M. & Humphreys, E., 2012. Nazca-South America interactions and the late Eocene-late Oligocene flat-slab episode in the central Andes, *Tectonics,* **31,** TC2013, doi:10.1029/2011TC003036.

Olbertz, D., Wortel, M. & Hansen, U., 1997. Trench migration and subduction zone geometry, *Geophys. Res. Lett.,* **24,** 221–224.

Oncken, O., Kley, J., Elger, K., Victor, P. & Schemmann, K., 2006. *Deformation of the Central Andean Upper Plate System—Facts, Fiction, and Constraints for Plateau Models,* Springer, 569 pp.

Pennington, W., 1984. The effect of oceanic crustal structure on phase-changes and subduction, *Tectonophysics,* **102,** 377–398.

Phillips, K. *et al.*, 2012. Structure of the subduction system in southern Peru from seismic array data, *J. geophys. Res.,* **117,** doi:10.1029/2012JB009540.

Pilger, R., 1981. Plate reconstructions, aseismic ridges, and low-angle subduction beneath the Andes, *Bull. seism. Soc. Am.,* **92,** 448–456.

Ryan, J., Ward, K., Porter, R., Beck, S., Zandt, G., Wagner, L., Minaya, E. & Tavera, H., 2011. Preliminary results from the CAUGHT experiment: investigation of the north central Andes subsurface using receiver functions and ambient noise tomography, in *AGU, Fall Meeting 2011,* abstract #T11B-2323.

Sacks, I., 1983. The subduction of young lithosphere, *J. geophys. Res.,* **88,** 3355–3366.

Schneider, J.F. & Sacks, I.S., 1987. Stress in the contorted Nazca Plate beneath southern Peru from local earthquakes, *J. geophys. Res.,* **92**(B13), 13 887–13 902.

Skinner, S.M. & Clayton, R.W., 2013. The lack of correlation between flat slabs and bathymetric impactors in South America, *Earth planet. Sci. Lett.,* **371–372,** 1–5.

Suarez, G., Molnar, P. & Burchfiel, B.C., 1983. Seismicity, fault plane solutions, depth of faulting, and active tectonics of the Andes of Peru, Ecuador, and southern Colombia, *J. geophys. Res.,* **88**(B12), 10 403–10 428.

Swenson, J., Beck, S.L. & Zandt, G., 2000. Crustal structure of the Altiplano from broadband regional waveform modeling: implications for the composition of thick continental crust, *J. geophys. Res.,* **105**(B1), 607–621.

van Hunen, J., van den Berg, A. & Vlaar, N., 2002a. The impact of the South American plate motion and the Nazca Ridge subduction on the flat subduction below south Peru, *Geophys. Res. Lett.,* **29**(14), doi: 10.1029/2001GL014004.

van Hunen, J., van den Berg, A. & Vlaar, N., 2002b. On the role of subducting oceanic plateaus in the development of shallow flat subduction, *Tectonophysics,* **352,** 317–333.

van Hunen, J., van den Berg, A. & Vlaar, N., 2004. Various mechanisms to induce present-day shallow flat subduction and implications for the younger Earth: a numerical parameter study, *Phys. Earth planet. Inter.,* **146,** 179–194.

von Huene, R., Corvalan, J., Flueh, E.R., Hinz, K., Korstgard, J., Ranero, C.R. & Weinrebe, W., the Condor Scientists, 1997. Tectonic control of the subducting Juan Fernandez Ridge on the Andean margin near Valparaiso, Chile, *Tectonics,* **16,** 474–488.

Whitman, D., Isacks, B.L. & Kay, S.M., 1993. *Lithospheric Structure and Along-Strike Segmentation of the Central Andean Plateau,* 17–29°S, in Proceedings of the Second ISAG, Oxford (UK), 21–23/9/1993.

Yan, Z. & Clayton, R.W., 2007. Regional mapping of the crustal structure in southern California from receiver functions, *J. geophys. Res.,* **112,** B05311, doi:10.1029/2006JB004622.

Yogodzinski, G.M., Lees, J.M., Churikova, T.G., Dorendorf, F., Woerner, G. & Volynets, O.N., 2001. Geochemical evidence for the melting of subducting oceanic lithosphere at plate edges, *Nature,* **409,** 500–504.

Yuan, X., Sobolev, S.V. & Kind, R., 2002. Moho topography in the central Andes and its geodynamic implications, *Earth planet. Sci. Lett.,* **199,** 389–402.

Zandt, G. & Ammon, C., 1995. Continental crust composition constrained by measurements of crustal Poisson's ratio, *Nature,* **374,** 152–154.

Zandt, G., Velasco, A. & Beck, S., 1994. Composition and thickness of the southern Altiplano crust, Bolivia, *Geology,* **22,** 1003–1006.

Zhu, L. & Kanamori, H., 2000. Moho depth variation in southern California from teleseismic receiver functions, *J. geophys. Res.,* **105**(B2), 2969–2980.

SUPPORTING INFORMATION

Additional Supporting Information may be found in the online version of this article:

Supplemental figures. This section contains supplementary material and figures to provide additional details and clarification of the methods and results discussed in the paper. (http://gji.oxfordjournals.org/lookup/suppl/doi:10.1093/gji/ggt504/-/DC1)

Please note: Oxford University Press is not responsible for the content or functionality of any supporting materials supplied by the authors. Any queries (other than missing material) should be directed to the corresponding author for the article.